

Imprints of Black Hole Shadows and Polarization Patterns of Various Thick Disks: Bumblebee gravity

Muhammad Israr Aslam,^{1,*} Nazek Alessa,^{2,†} Chen-Yu Yang,^{3,‡} and Xiao-Xiong Zeng^{4,§}

¹*Department of Mathematics, School of Science,
University of Management and Technology, Lahore-54770, Pakistan.*

²*Department of Mathematical Sciences, College of Science,
Princess Nourah bint Abdulrahman University,
P.O.Box 84428, Riyadh 11671, Saudi Arabia*

³*Department of Mechanics, Chongqing Jiaotong University,
Chongqing 4000, People's Republic of China*

⁴*College of Physics and Optoelectronic Engineering,
Chongqing Normal University, Chongqing 401331, People's Republic of China*

(Dated: May 26, 2026)

The main objective of this study is to explore the shadow and polarization patterns of a Kerr-Sen-like BH induced from Bumblebee gravity, which, among other alternative theories of gravity beyond Einstein gravity, stands out as a promising candidate for explaining certain high-energy astrophysical phenomena. Specifically, we would like to probe the influence of the rate of LSB parameter ℓ and the Bumblebee charge Q on the resulting image morphology at 230GHz. We adopt a phenomenological RIAF-like model and an analytical BAAF disk model. Both models depict that the bright ring is encircled by two central dark regions, each of which gradually shrinks with increasing ℓ . Consequently, frame-dragging gives rise to a pronounced brightness asymmetry, which is more enhanced with increasing Q . A notable feature in the anisotropic emission case is the emergence of a vertically stretched, elliptical ring structure. Compared with the RIAF framework, the bright ring in the BAAF disk images appears geometrically thinner, and the separation between the primary and higher-order images becomes more pronounced. Finally, the polarization patterns trace the brightness distribution and vary with both ℓ and Q , reflecting the spacetime structure. These results demonstrate that intensity and polarization in thick disk models provide probes of Kerr-Sen-like BHs and near-horizon accretion physics

*mrisraraslam@gmail.com, israr.aslam@umt.edu.pk

†naalessa@pnu.edu.sa

‡chenyu_yang2024@163.com

§xxzengphysics@163.com (Corresponding author)

I. INTRODUCTION

Recent experimental development in the fabric of gravitational physics has ushered in a new window in which electromagnetic radiation is used to probe the nature of ultra-compact objects, including BHs. Among the most significant breakthroughs are the discoveries by the Event Horizon Telescope (EHT), which imaged the electromagnetic emission from super-heated plasma orbiting the supermassive objects at the center of both the M87 and Milky Way galaxies [1–4]. Complementing these achievements, the GRAVITY instrument has detected infrared flares in the immediate vicinity of our Galactic center [5, 6]. This emerging observational window enables the gravitational physics community to rigorously test theoretical models through the imaging of BHs, particularly by comparing observations with General Relativistic Magneto-Hydrodynamic (GRMHD) simulations of the surrounding plasma [7, 8].

The solution of Kerr BH serves as a fundamental cornerstone for several fundamental theorems within the framework of general relativity (GR), which establish it as the unique stationary and axisymmetric vacuum solution of the Einstein field equations endowed with Killing horizons [9]. Moreover, recent EHT experimental achievements are consistent with the theoretical predictions of the Kerr hypothesis [10, 11]. Based on this hypothesis, the complete gravitational collapse of a body in a realistic astrophysical setting leads to the formation of a rotating, electrically neutral BH [12, 13]. Consequently, the Kerr paradigm has emerged as the standard mechanism against which observational data are interpreted, while alternative space-times describing exotic compact objects must demonstrate superior agreement with observations to be considered viable [14, 15]. In this perspectives, despite the good agreement of GR with observational constraints, this theory still faces several significant challenges, specifically when integrated with the Standard Model of particle physics, leading to the pursuit of modified theories of gravity. These challenges leave open the room of probing new physics beyond GR within the limits of current precision. Among various extensions, Lorentz symmetry breaking (LSB) has emerged as a promising window into the potential quantum nature of gravity at the Planck scale [16, 17].

Although Lorentz symmetry serves as a fundamental cornerstone of both quantum field theory and GR, its exact validity across all energy scales remains an open question. Many exciting theories of quantum gravity suggest that this symmetry may be violated at sufficiently high-energy scales [18, 19], potentially giving rise to observable signatures in low-energy effective descriptions [20]. In this regard, the authors in [21] construct the Standard Model Extension mechanism, to systematically characterize the LSB effects, which provide a unified framework for describing

Lorentz violation. From the gravity perspectives, the Einstein-Bumblebee model stands as one of the simplest implementations of the Standard Model Extension [18, 22, 23]. It induces spontaneous LSB by defining a vector field with a non-zero vacuum expectation value. In this scenario, using the mechanism of Einstein-Bumblebee gravity model, many BH solutions have been derived, for instance one can see Refs. [24–28]. Among them, a Kerr-Sen-like BH solution ¹ has been obtained from the Einstein-Bumblebee action, in which two extra parameters, corresponding to the rate of Lorentz symmetry breaking L and the charge in Kerr-Sen BH Q , are spontaneously added [24, 27, 30, 31]. The observational constraints of these two parameters were carefully investigated from the observations of supermassive BHs [32–36]. More recently, several significant properties of BH solutions have been explored in the context of Bumblebee gravity model such as, energy extraction via magnetic reconnection [37], shadow observables [38], vacuum solutions [39], thermodynamics [40] dark matter spike [41] and the process of accretion disk [42] etc.

The BH shadow is a dark region formed by the deflection of light in the strong gravitational field of a BH. Its morphology and radius are primarily evaluated by the underlying space-time geometry, allowing one to infer the significant properties of BHs with the analysis of shadow dynamics and its associated consequences. Continued advancements in experimental physics and observational astronomy have significantly deepened our understanding of BHs. It is widely acknowledged that when matter is captured by the gravitational field of a rotating supermassive BH, frame-dragging effects compel the particles to co-rotate with the BH. Subsequently, the infalling matter forms a hot, magnetized plasma that radiate thermal synchrotron radiation, producing a luminous accretion disk. And for rapidly spinning BHs, electromagnetic energy extraction mechanisms can further drive relativistic outflows [43], which is known as funnel-wall jets. The base of the jet is enveloped by the jet sheath that generates substantial thermal synchrotron emission. As a result, the radiation observed in BH images may arise from both the accretion flow and the jet. In recent years, considerable attention has been devoted toward a range of accretion disk models, including spherical accretion models [44–48], geometrically thin accretion disks [49–54], and Einstein rings in holography [55–58].

As the central engines of many low-luminosity active galactic nuclei, supermassive BHs are often embedded in magnetized, advection-dominated accretion matter [59, 60]. In these environments, the plasma is characterized by strong radial inflow and weak Coulomb coupling between ions and

¹ A charged and rotating BH solution was proposed under the scheme of heterotic string theory, which is well-known as the Kerr-Sen BH [29].

electrons [61]. General-relativistic magnetohydrodynamic (GRMHD) simulations, although computationally intensive, provide the most self-consistent mechanism currently available for studying these accretion flows [62], and can be investigated in modified theories [63, 64]. In this scenario, various studies considers the radiatively inefficient accretion flow (RIAF) model with relatively low radiation efficiency, in which the vertically averaged electron number density and temperature typically follow a power-law distribution with radius [65–68].

On the other hand, semi-analytic accretion models continue to play a valuable complementary role. They allow for efficient exploration of parameter space and enable controlled investigations that isolate specific physical processes [69, 70]. However, many such models are built on simplifying assumptions, such as self-similar radial profiles, geometrically thin disks, or nearly circular orbits that may break down in the strongly relativistic regions close to the event horizon. In the immediate vicinity of the event horizon, gravity dominates the dynamics, making the ballistic approximation treating the plasma motion as timelike geodesics, provides a useful and analytically manageable description of the flow [71, 72]. Based on this mechanism, Hou et al. [73] developed a self-consistent model (known as ballistic approximation accretion flow (BAAF) model) in Kerr spacetime, which provides explicit expressions for thermodynamic quantities and magnetic field configurations. Consequently, this model provides a physically consistent mechanism for describing the structure and dynamics of geometrically thick accretion flows, and enabling comprehensive investigation of polarization characteristics in the near horizon region.

The thermal synchrotron radiation radiated by electrons in BH accretion flows having different polarization properties. The polarization vector is perpendicular to both the magnetic field and the direction of wave propagation, aligning with the electric field vector. In the intense gravitational field, this vector is carried along null geodesics through parallel transport and forming the polarized image of the accretion flow on the observer’s screen. As a result, polarimetric measurements serve as a powerful probe of the plasma behavior and magnetic field geometry in the vicinity of BHs [74]. Recent polarization images released by EHT have display a prominent polarization structures within emission rings [75, 76]. Using the approximate analytic ray-tracing formalism [77], in 2021, EHT regenerated both the electric vector position angle (EVPA) distribution and the relative polarization intensity of M87* [78]. In this perspectives, the shadows and polarization images of various BH models, including horizonless ultra compact objects, have been extensively explored in the literature [79–91]. Building upon this framework, we extend the analysis to Kerr-Sen-like metric in Einstein-Bumblebee gravity and investigate the associated consequences for BH imaging illuminated by a thick accretion flow. For desired results, we consider RIAF and

BAAF accretion models. We examine how the LSB parameter ℓ , the charge parameter Q , and the observer inclination modulates key flow properties, including the density profile, thermal structure, and magnetic-field configuration. We further examine the polarization properties and explore how these parameters influence the polarization structure near the event horizon.

The remaining parts of this paper are structured as follows. In sect. **II**, we briefly define the Kerr-Sen-like metric coming from Einstein-Bumblebee gravity and the corresponding geodesics equations including the definition of photon spheres. In sect. **III**, we describe the fundamental mechanism responsible for synchrotron radiation and the covariant form of the radiative transfer equation, including both the isotropic and anisotropic radiation models. Section **IV** reflects the background of the accretion flow models consists of RIAF and BAAF frameworks. We outline the theoretical mechanism for polarization imaging within the BAAF model in sect. **V**. The last section offers our concluding remarks. Throughout this paper, we adopt the natural units with $G = M = c = 1$ without loss of generality.

II. KERR-SEN-LIKE BLACK HOLE AND NULL GEODESICS

We describe the Kerr-Sen-like BH metric, whose axisymmetric rotating BH solution in Boyer-Lindquist coordinates can be written as [27, 30, 37]

$$ds^2 = -\left(1 - \frac{2r}{\Sigma}\right)dt^2 + (1 + \ell)\frac{\Sigma}{\Delta}dr^2 + \Sigma d\theta^2 + \frac{A \sin^2 \theta}{\Sigma}d\phi^2 - \frac{4\tilde{A}r \sin^2 \theta}{\Sigma}dt d\phi, \quad (1)$$

where²

$$\Sigma = r(r + Q) + \tilde{A}^2 \cos^2 \theta, \quad \Delta = r(r + Q) - 2r + \tilde{A}^2, \quad A = [r(r + Q) + \tilde{A}^2]^2 - \tilde{A}^2 \Delta \sin^2 \theta, \quad (2)$$

with $\tilde{A} = a\sqrt{1 + \ell}$. Moreover, the parameter ℓ represents the LSB, and Q represent the charge parameter. In the framework of Einstein-Bumblebee gravity, Q can be regarded as the vacuum expectation value of the Bumblebee field, and $\ell \propto \varrho Q^2/a$, where ϱ is the coupling constant between the gravitational field and the Bumblebee field and a is the spin parameter [27, 30, 37]. The event horizons are determined by $\Delta/\Sigma = 0$, which yields

$$r_{\pm} = \frac{2 - Q \pm \sqrt{4 - 4\tilde{A}^2 - 4Q + Q^2}}{2}, \quad (3)$$

where r_+ and r_- correspond to the event horizon and the Cauchy horizon, respectively. Moreover, the spinning Kerr-Sen-like BH (1) exhibits time-translational and axial rotational symmetries,

² A more widely used notation is $\Delta = \frac{r(r+Q)-2r}{1+\ell} + a^2$.

which imply the presence of two corresponding Killing vector fields. To facilitate the study of BH shadow imaging, we employ the zero angular momentum observer (ZAMO) frame, defined as a stationary observer with vanishing angular momentum at infinity. However, due to the effect of frame dragging, the ZAMO still has a position dependent angular velocity $\omega = \frac{d\phi}{dt} = -\frac{g_{t\phi}}{g_{\phi\phi}}$. As the observer reaches the BH, ω increases and reaches its maximum at the event horizon $\Omega = \omega|_{r=r_+}$, in which Ω interpret the angular velocity of the BH. At this position, the observer's angular velocity ω coincides with Ω indicating a state of corotation. Now we evaluate the motion of light particles in the vicinity of spinning Kerr-Sen-like BH. Since the photon follows the null geodesics in a given BH spacetime, hence, for spacetime (1), the geodesic motion is governed by the Hamilton-Jacobi equation, which is given by [92]

$$\frac{\partial \tilde{\mathcal{I}}}{\partial \varpi} = -\frac{1}{2}g^{\mu\nu} \frac{\partial \tilde{\mathcal{I}}}{\partial x^\mu} \frac{\partial \tilde{\mathcal{I}}}{\partial x^\nu}, \quad (4)$$

here $\tilde{\mathcal{I}}$ indicates the Jacobi action and ϖ is the affine parameter of the trajectory curves. The Jacobi action $\tilde{\mathcal{I}}$ of the photon can be separated into the following form

$$\tilde{\mathcal{I}} = \frac{1}{2}\varrho^2\varpi - Et + L\phi + J_r(r) + J_\theta(\theta). \quad (5)$$

For photons $\varrho = 0$. The quantities $E = -p_t$ and $L = p_\phi$ represents the conserved energy and conserved angular momentum of the photon in the direction of rotation axis, respectively. The components $J_r(r)$ and $J_\theta(\theta)$ are arbitrary functions. In this regard, the geodesic equations can be written in first-order form

$$\begin{aligned} \Sigma^2 \frac{dt}{d\varpi} &= a(L - aE \sin^2 \theta) + \frac{r^2 + a^2}{\Delta} (E(r^2 + a^2) - aL), \\ \Sigma^2 \frac{dr}{d\varpi} &= \pm \sqrt{\tilde{R}(r)}, \\ \Sigma^2 \frac{d\theta}{d\varpi} &= \pm \sqrt{\Theta(\theta)}, \\ \Sigma^2 \frac{d\phi}{d\varpi} &= (L \csc^2 \theta - aE) + \frac{a}{\Delta} (E(r^2 + a^2) - aL). \end{aligned} \quad (6)$$

Here

$$\begin{aligned} \tilde{R}(r) &= (E(r^2 + a^2) - aL)^2 - \Delta(\tilde{Q} + (L - aE)^2), \\ \Theta(\theta) &= \tilde{Q} + (a^2 E^2 - L^2 \csc^2 \theta) \cos^2 \theta, \end{aligned} \quad (7)$$

are the radial and angular potentials, respectively, while \tilde{Q} is the Carter constant. On the equatorial plane, where $\theta = \pi/2$, the radial equation can be rewritten as $\dot{r}^2 + V_{\text{eff}} = 0$, where V_{eff} is the effective potential, which is defined as

$$V_{\text{eff}} = -\frac{\tilde{R}(r)}{r^4}. \quad (8)$$

For convenience, we define the dimensionless impact parameters of photons

$$\xi = \frac{L}{E}, \quad \eta = \frac{\tilde{Q}}{E^2}. \quad (9)$$

The photon sphere radius r_p can be evaluated from the radial potential and its derivative as [92]

$$\tilde{R}(r)|_{r=r_p} = 0, \quad \partial_r \tilde{R}(r)|_{r=r_p} = 0. \quad (10)$$

Considering a photon captured by the BH, those residing on stable orbits remain bound for infinitely, whereas photons on unstable orbits may eventually escape after circling the BH for some time. The conditions for such unstable orbits are given by

$$\partial_r^2 V_{\text{eff}}|_{r=r_p} < 0. \quad (11)$$

III. SYNCHROTRON RADIATION AND RADIATIVE TRANSFER

We consider the presence of a magnetic field in the vicinity of the BH, the explicit configuration of which will be specified in subsequent sections. Within this field, both thermal and nonthermal electrons in the accreting plasma emit synchrotron radiation as they are accelerated by the Lorentz force. Our investigation is primarily concerned with synchrotron emission arising from highly relativistic electrons. In this section, we present an overview of the fundamental mechanism responsible for synchrotron radiation in the surrounding plasma and describe the propagation of the emitted photons from their source to the observer's image plane. All physical quantities are expressed in CGS units. For unpolarized environment, the covariant form of the radiative transfer equation is [94]

$$\frac{d}{d\varpi} I = J - \lambda I. \quad (12)$$

where, I , J , and λ are Lorentz invariant quantities. For an arbitrary observer, let ν represents the photon frequency measured in the observer's frame. The relations between these invariants are defined as

$$I = \frac{I_\nu}{\nu^3}, \quad J = \frac{j_\nu}{\nu^2}, \quad \lambda = \nu \lambda_\nu. \quad (13)$$

in which I_ν is the specific intensity, j_ν is the emissivity, and λ_ν is the absorption coefficient. The solution of Eq. (12) is

$$I(\varpi) = I(\varpi_0) + \int_{\varpi_0}^{\varpi} d\varpi' J(\varpi') \exp\left(-\int_{\varpi'}^{\varpi} d\varpi'' \lambda(\varpi'')\right). \quad (14)$$

To ensure consistency with the unit system adopted in Eq. (13), we recast the equation in the Centimeter-Gram-Second (CGS) system of units. For this purpose, we rescale the affine parameter ϖ appearing in Eq. (12) according to the transformation $\frac{d}{d\varpi} \rightarrow \frac{1}{C} \frac{d}{d\varpi}$, where $C = \frac{r_g}{\nu_0}$. Here, $r_g = \frac{GM}{c^2}$ denotes the gravitational radius of the black hole, and ν_0 represents the photon frequency as measured by an observer at infinity. With this rescaling, the equation takes the following form

$$\frac{1}{C} \frac{d}{d\varpi} I = J - \lambda I, \quad (15)$$

with the corresponding solution

$$I_\nu = g^3 I_{\nu_0} + r_g \int_{\varpi_0}^{\varpi} d\varpi' g^2 j_\nu(\varpi') \exp\left(-r_g \int_{\varpi'}^{\varpi} d\varpi'' \frac{\lambda_\nu(\varpi'')}{g}\right). \quad (16)$$

Here, $g = \nu_0/\nu$ is the redshift factor, and ν corresponds to the photon frequency measured in the local static frame. For explicit expression of g , we define the fluid four velocity be u^α and the photon four-momentum be k_α with $k_t = -1$, then

$$g = \frac{k_\alpha (\partial_t)^\alpha}{k_\alpha u^\alpha} = \frac{k_t}{k_\alpha u^\alpha} = -\frac{1}{k_\alpha u^\alpha}. \quad (17)$$

From the above relations, it is evident that both the emissivity and the absorption coefficient must be specified in order to accurately evaluate the observed intensity. We notice that the radiative coefficients j_ν and λ_ν as defined in Eq. (13) closely depend on the specific emission mechanism, with different physical processes leading to distinct functional forms of j_ν and λ_ν . In present analysis, we focus on synchrotron radiation produced by electrons in the ultra-relativistic regime, expressed in CGS units. Throughout this section, c denotes the speed of light, h is the Planck constant, e is the elementary charge, and k_B represent the Boltzmann constant, while the local magnetic field is represented by b^α .

In a plasma system, synchrotron radiation is mainly participated by electrons, and its emissivity j_ν plays a major role in thick disk imaging, given explicitly by

$$j_\nu = \frac{\sqrt{3}e^3 B \sin \theta_B}{4\pi m_e c^2} \int_0^\infty d\tau N(\tau) F\left(\frac{\nu}{\nu_s}\right). \quad (18)$$

Here, $\tau = \frac{1}{\sqrt{1-\beta^2}}$ denotes the Lorentz factor of the charged particle, $N(\tau)$ corresponds to the electron configuration function, and $F(x)$ is expressed as

$$F(x) = x \int_x^\infty dy K_{5/3}(y), \quad (19)$$

where $K_n(x)$ is the modified Bessel function of the second kind of order n . The angle θ_B between the spatial projection of the photon four-momentum $e_{(k)}^\alpha$ and the magnetic field direction $e_{(b)}^\alpha$ is

$$\theta_B = \arccos \left(e_{(b)}^\alpha \cdot e_{(k)}^\alpha \right) = \arccos \left[\frac{g}{B} (b_\alpha k^\alpha) \right], \quad (20)$$

with

$$e_{(k)}^\alpha = - \left(\frac{k^\alpha}{u^\nu k_\nu} + u^\alpha \right), \quad e_{(b)}^\alpha = \frac{b^\alpha}{B}. \quad (21)$$

Here, $B = \sqrt{b_\alpha b^\alpha}$ is the magnitude of the local magnetic field. In Eq. (18), the characteristic frequency ν_s is

$$\nu_s = \frac{3eB\tau^2 \sin \theta_B}{4\pi m_e c}. \quad (22)$$

Different electron distributions give rise to distinct emissivities. For a thermal electron population, the distribution function $N(\tau)$ takes the following form

$$N(\tau) = \frac{n_e \beta \tau^2}{\theta_e K_2(\theta_e^{-1})} e^{-\tau/\theta_e}, \quad (23)$$

where n_e is the electron number density, $\theta_e = k_B T_e / m_e c^2$ is the dimensionless electron temperature, and T_e denotes the thermodynamic temperature of electrons. In the extreme relativistic limit, $\beta \approx 1$ and $\theta_e \gg 1$, the asymptotic form $K_2(\frac{1}{\theta_e}) \approx 2\theta_e^2$ holds. Defining $z = \tau/\theta_e$, Eq. (18) becomes as

$$j_\nu = \frac{\sqrt{3} n_e e^3 B \sin \theta_B}{8\pi m_e c^2} \int_0^\infty z^2 e^{-z} F \left(\frac{\nu}{\nu_s} \right) dz. \quad (24)$$

Defining $x = (\nu/\nu_s) z^2$, the emissivity can be defined as

$$j_\nu = \frac{\sqrt{3} n_e e^2 \nu}{6c\theta_e^2} \mathcal{I}(x), \quad x = \frac{\nu}{\nu_c}, \quad \nu_c = \frac{3eB\theta_e^2 \sin \theta_B}{4\pi m_e c}, \quad (25)$$

where $\mathcal{I}(x)$ is the dimensionless function, which is defined as

$$\mathcal{I}(x) = \frac{1}{x} \int_0^\infty z^2 e^{-z} F \left(\frac{x}{z^2} \right) dz. \quad (26)$$

Since this function does not admit a closed-form expression in terms of elementary functions, it is approximated using an appropriate fitting formula. In this manuscript, we consider two radiation models: isotropic and anisotropic radiation. We first discuss the isotropic radiation model. For isotropic radiation, only the magnitude of the magnetic field is considered, ignoring its direction. The angle averaged synchrotron emissivity is defined by

$$\bar{j}_\nu = \frac{1}{2} \int_0^\pi j_\nu \sin \theta_B d\theta_B. \quad (27)$$

Its corresponding fitting formula, as provided in Ref. [95], reads

$$\bar{j}_\nu = \frac{ne^2\nu}{2\sqrt{3}c\theta_e^2}\mathbb{M}(x), \quad x = \frac{\nu}{\nu_c}, \quad \nu_c = \frac{3eB\theta_e^2}{4\pi m_e c}, \quad (28)$$

where the dimensionless function $\mathbb{M}(x)$ is given by

$$\mathbb{M}(x) = \frac{4.0505}{x^{1/6}} \left(1 + \frac{0.4}{x^{1/4}} + \frac{0.5316}{x^{1/2}} \right) \exp\left(-1.8899x^{1/3}\right). \quad (29)$$

Next, we consider an anisotropic radiation model. In this mechanism, the magnetic field is assumed to consist of a combination of toroidal and poloidal components, such that the magnetic four-vector can be expressed as follows

$$b^\alpha \sim (l, 0, 0, 1), \quad (30)$$

with

$$l = -\frac{u_\phi}{u_t}, \quad u_\nu = g_{\alpha\nu}u^\alpha = (u_t, u_r, u_\theta, u_\phi). \quad (31)$$

The magnetic field is perpendicular to the fluid four velocity, satisfying $u^\alpha b_\alpha = 0$. The emissivity for the anisotropic radiation model is given by Eq. (25), i.e.,

$$j_\nu = \frac{n_e e^2 \nu}{2\sqrt{3}c\theta_e^2} \mathcal{I}(x), \quad x = \frac{\nu}{\nu_c}, \quad \nu_c = \frac{3eB\theta_e^2 \sin\theta_B}{4\pi m_e c},$$

where the dimensionless function $\mathcal{I}(x)$ is given in Ref. [96] as

$$\mathcal{I}(x) = 2.5651 \left(1 + 1.92x^{-1/3} + 0.9977x^{-2/3} \right) \exp\left(-1.8899x^{1/3}\right). \quad (32)$$

For a thermal electron distribution, the absorption process satisfies Kirchhoff's law, so that the absorption coefficient λ_ν obeys

$$\lambda_\nu = \frac{j_\nu}{\mathcal{B}_\nu}, \quad \mathcal{B}_\nu = \frac{2h\nu^3}{c^2} \frac{1}{\exp\left(\frac{h\nu}{k_B T_e}\right) - 1}, \quad (33)$$

where, \mathcal{B}_ν is the Planck black-body function. For numerical simulations, we express the following constants, as

$$C_1 = \frac{\sqrt{3}e^2 n_h \nu_h}{6\theta_h^2 c}, \quad C_2 = \frac{4\pi c m_e \nu_h}{3e B_h \theta_h^2}, \quad C_3 = \frac{h\nu_h}{m_e \theta_h c^2}, \quad C_4 = \frac{2h\nu_h^3}{c^2}, \quad C_5 = \sqrt{c^2 n_h m_p}, \quad (34)$$

in which, n_h , θ_h , ν_h , and B_h corresponds to the values of the electron number density, the dimensionless electron temperature, the photon frequency, and the local magnetic field strength at the

event horizon, respectively. Particularly, we set $\nu_h = 10^9$ Hz = 1 GHz and $B_h = 1$. Based on this parameterization, the emissivity and the black-body function can be defined as

$$j_\nu = \frac{C_1 \hat{n}_e \hat{\nu} I(x)}{\hat{\theta}_e^2}, \quad x = \frac{C_2 \hat{\nu}}{\hat{B} \hat{\theta}_e^2 \sin \theta_B}, \quad \mathcal{B}_\nu = \frac{C_4 \hat{\nu}^3}{\exp\left(\frac{C_3 \hat{\nu}}{\hat{\theta}_e}\right) - 1}, \quad (35)$$

here $\hat{\nu} = \nu/\nu_h$, $\hat{n}_e = n_e/n_h$, $\hat{B} = B/B_h$, and $\hat{\theta}_e = \theta_e/\theta_h$. Using Eqs. (33) and (35), one can compute the intensity in Eq. (16). However, the electron number density and temperature appearing in these expressions remain unspecified. In the following section, we outline how these quantities are determined within the context of different accretion flow models.

IV. DISK MODELS

For unpolarized imaging, we examine two geometrically thick and optically thin accretion flow models, well-known as RIAF model [97] and the BAAF model [73, 98]. The RIAF model is broadly consistent with GRMHD simulations and has demonstrated considerable success in reproducing the overall morphology of M87* [1]. However, its applicability to polarization studies remains limited, as it neglects key physical ingredients such as outflows, non-thermal particles, and the full dynamical structure captured by GRMHD frameworks. To overcome these limitations, we adopt the BAAF model, which assumes that fluid acceleration in the vicinity of the event horizon is predominantly governed by gravitational effects. This model provides explicit prescriptions for the thermodynamic variables and magnetic field configuration, enabling a more realistic and self-consistent description of the morphology and dynamics of geometrically thick accretion flows in the near-horizon region of the BH.

A. Density and Temperature

We impose a cylindrical coordinate system, where the cylindrical radius is given by $R = r \sin \theta$ and the height above the equatorial plane ($\theta = \pi/2$) is $z = r \cos \theta$. Closely followed by [97], in RIAF model, the density and temperature profiles can be expressed as

$$n_e = n_h \left(\frac{r}{r_+}\right)^2 \exp\left(-\frac{z^2}{2R^2}\right), \quad T_e = T_h \left(\frac{r}{r_+}\right), \quad (36)$$

where n_h and T_h are the electron number density and temperature at the outer horizon, respectively. The magnetic field magnitude is defined via the cold magnetization parameter $\eta = \frac{b^2}{\rho} = \frac{b^2}{n_e m_p c^2}$ as $b = \sqrt{\eta \rho}$, where $\rho = n_e m_p c^2$ is the fluid mass density, and $\eta \sim 0.1$ [99]. Here, we consider both the

isotropic radiation (27) and anisotropic radiation (25) mechanism. After specifying the fundamental properties of the accretion flow motion, we proceed to describe its dynamics. In general, the fluid motion may be modeled as free-fall, circular motion around the BH, or a combination of both. In the present work, we primarily focus on the free-fall scenario. Under the assumption that the fluid is initially at rest at infinity, the corresponding four-velocity can be written as:

$$u_t = -g^{tt}, \quad u^r = -\sqrt{-(1 + g^{tt})g^{rr}}. \quad (37)$$

The four-velocity must be a timelike vector throughout the entire space-time, requiring $g^{tt} \leq -1$. After establishing the fundamental properties and dynamics of the accreting matter, we proceed to describe the behavior of electrons through the radiative transfer equation. Further, we employ a ray-tracing method combined with a ZAMO frame and celestial coordinates to establish the mapping between pixel coordinates on the projection screen and celestial coordinates. This provides a solid computational foundation for BH imaging studies. For comprehensive review, one can see Refs. [51, 79].

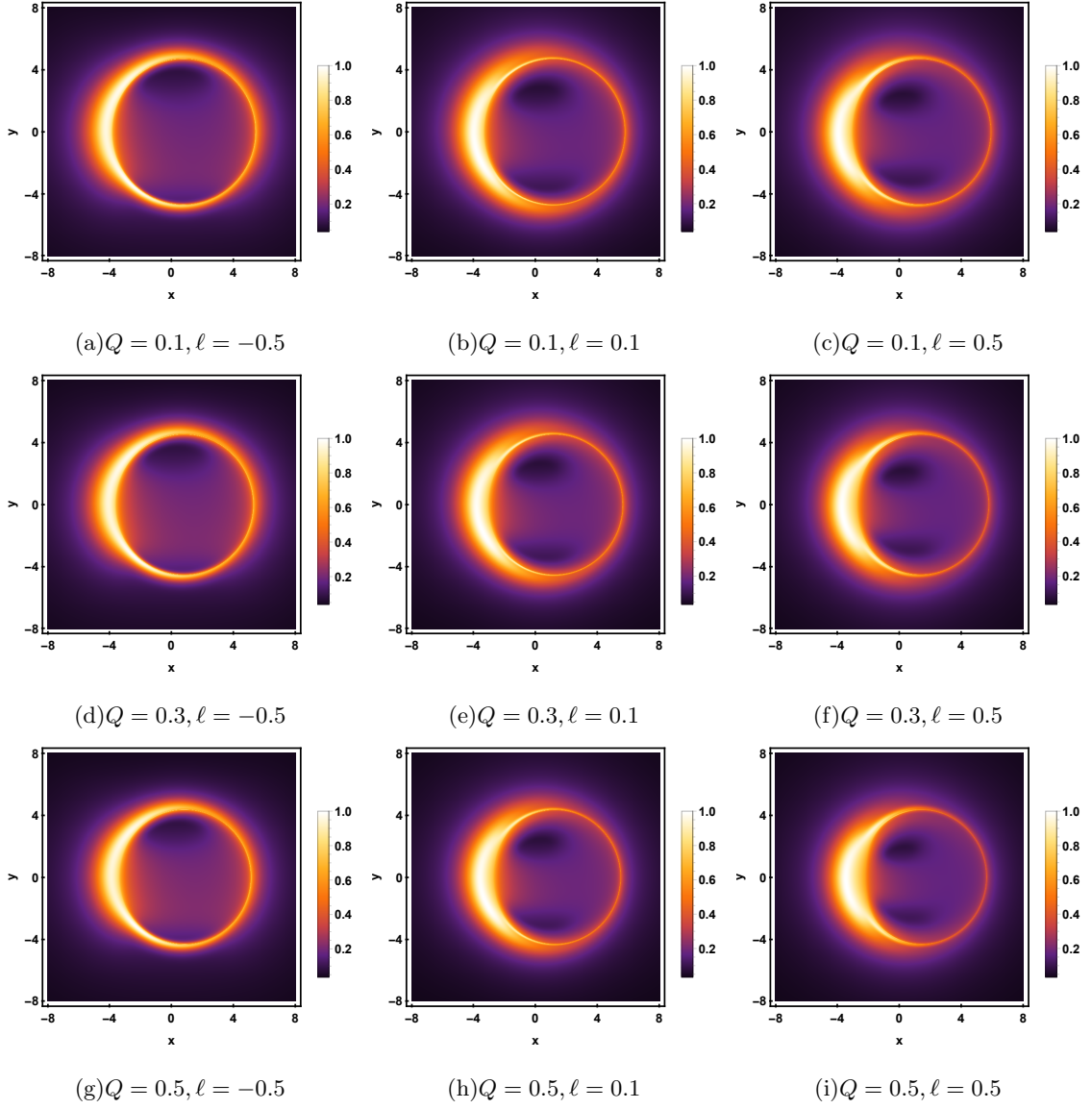


FIG. 1: Imaging results of the thick accretion disk for isotropic radiation under the RIAF model, and the accretion flow follows the infalling motion. The observation is performed at a frequency of 230GHz with an inclination angle of $\theta_o = 75^\circ$, and a spin parameter $a = 0.6$.

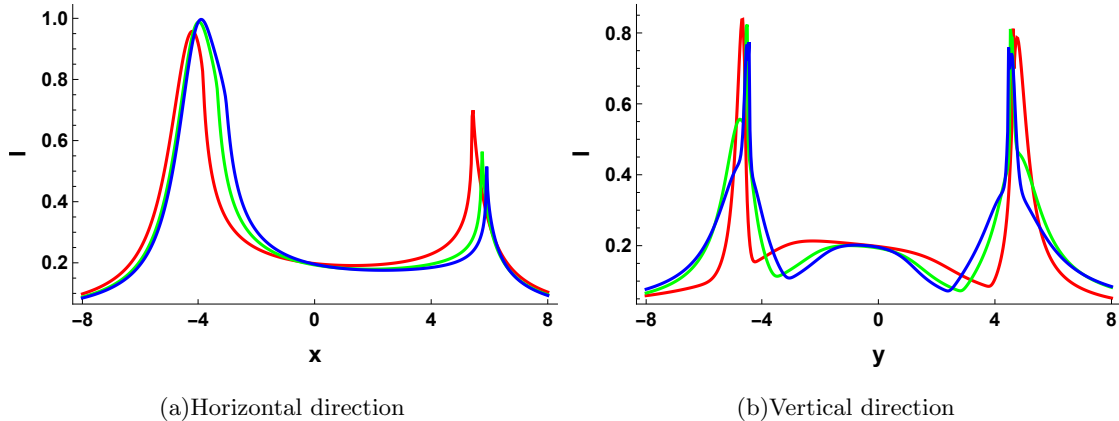


FIG. 2: Intensity distribution for isotropic radiation under the RIAF model, and the accretion flow follows the infalling motion. The red, green and blue curves corresponds to $\ell = -0.5, 0.1$ and 0.5 , respectively with a fixed $a = 0.6, Q = 0.1, \theta_o = 75^\circ$.

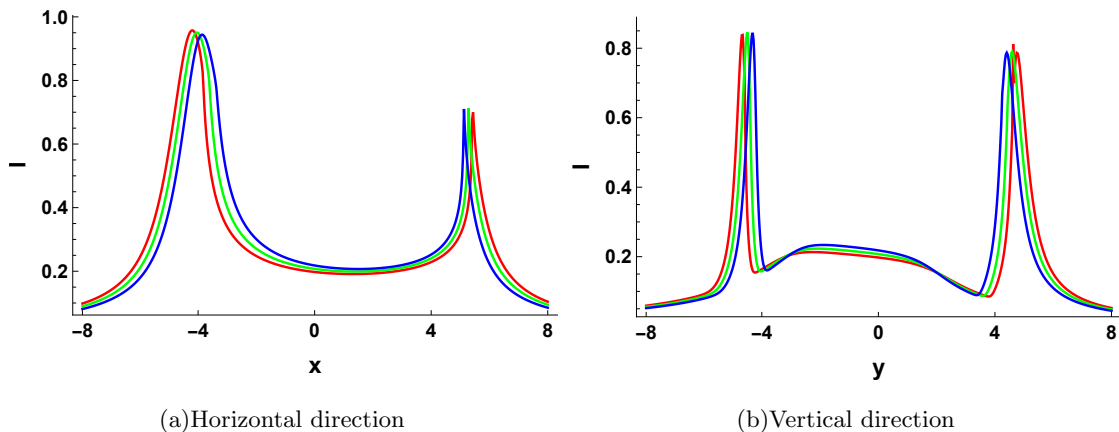


FIG. 3: Intensity distribution for isotropic radiation under the RIAF model, and the accretion flow follows the infalling motion. The red, green and blue curves corresponds to $Q = 0.1, 0.3$ and 0.5 , respectively with a fixed $a = 0.6, \ell = -0.5, \theta_o = 75^\circ$.

In Fig. 1, we interpret the shadow images of Kerr-Sen-like BH with isotropic radiation under RIAF model. The observation is performed at a frequency of 230GHz with an inclination angle of $\theta_o = 75^\circ$, and a spin parameter $a = 0.6$. The accretion flow follows the infalling motion inspired by ballistic approximation. From left to right, the image plots for the values of LSB parameter ℓ are $-0.5, 0.1$, and 0.5 , respectively. Whereas, from top to bottom, the image plots for the values of charge parameter Q are $0.1, 0.3$, and 0.5 , respectively. Analysis of Fig. 1 shows that all images exhibit a bright ring structure, corresponding to higher-order images, in which photons orbit the BH one or multiple times before reaching the observer. This feature is a direct manifestation of strong gravitational lensing. Beyond of this ring-like structure, there are regions with nonzero

intensity corresponding to the primary image, where photons travel directly from the accretion flow to the observer without orbiting the BH. Moreover, regardless of parameter alterations, there are regions of reduced intensity inside the higher-order images. This region originates from the event horizon of the BH. For geometrically thin accretion disk, the accreting matter is confined to the equatorial plane, so the event horizon appears as a dark region, which is well-known as “inner shadow”, and may be captured by EHT [100]. On the contrary, for geometrically thick accretion disks, radiation from outside the equatorial plane may partially obscure this region, making it less distinguishable. Compared to thin disks, thick disks are more physically realistic, which explains why direct imaging of BH event horizons remains challenging.

From the first row of Fig. 1, when $Q = 0.1$ (see first row), the higher-order images of BH exhibits a “D”-shape in the left side of the screen, which is significantly enhanced intensity with increasing ℓ . As Q increases to 0.3 (see second row), the intensity of higher-order images are more pronounced in the left side of the screen, which is increases with increasing ℓ . When Q further increases to 0.5 (see third row), a crescent-shaped bright region appears on the left side of the image, which is significantly enhanced with the aid of ℓ . Interestingly, when $\ell = 0.1$, two dark regions appear inside the higher-order image, with the upper region slightly darker than the lower one, which is more obvious when $\ell = 0.5$. This phenomenon arises from gravitational lensing effects. In summary, increasing Q slightly decreases both the size and brightness of the higher-order image, while increasing ℓ alters the shape of the higher-order image and obscure the horizon’s outline. Additionally, the image is nearly symmetric in the vertical direction, although the left-right intensity remains higher than the top-bottom intensity. This vertical intensity dependence reflects the equatorial symmetry of the thick disk: for observers near the equatorial plane, high-latitude radiation partially fills the dark regions, while for near-polar observers, photons reaching the observer are relatively insufficient.

For a better understanding about Fig. 1, we have plotted Figs. 2 and 3, which exhibits the corresponding intensity distributions along the x -axis and y -axis of the observer’s screen. All panels in Fig. 1 exhibit a pronounced bright ring, corresponding to the peaks in Figs. 2 and 3. Comparing the rows of Fig. 1 with Fig. 2, we observe that for a fixed value of Q , both the bright ring and central region are slightly reduces with the augmentation of ℓ . Additionally, due to the frame-dragging effect induced by LSB parameter ℓ , the intensity on the left side of the image becomes significantly enhanced with increasing ℓ . On the contrary, by comparing the columns of Fig. 1 with those of Fig. 3, we observe that, for a fixed value of ℓ , both the bright ring and the central dark region slightly shrink as Q increases. Additionally, the width of the ring decreases

marginally.

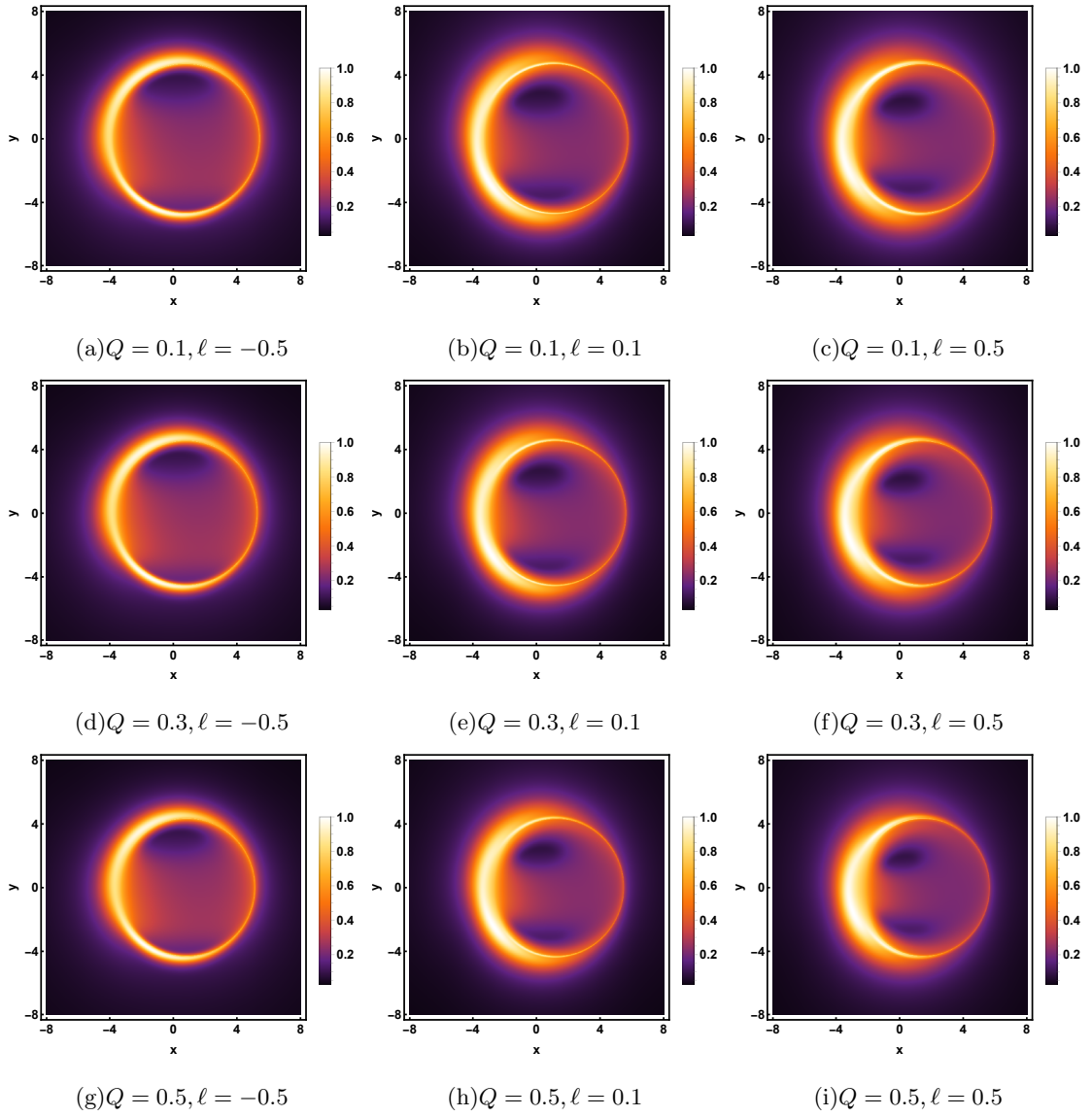


FIG. 4: Imaging results of the thick accretion disk for anisotropic radiation under the RIAF model, and the accretion flow follows the infalling motion. The observation is performed at a frequency of 230GHz with an inclination angle of $\theta_o = 75^\circ$, and a spin parameter $a = 0.6$.

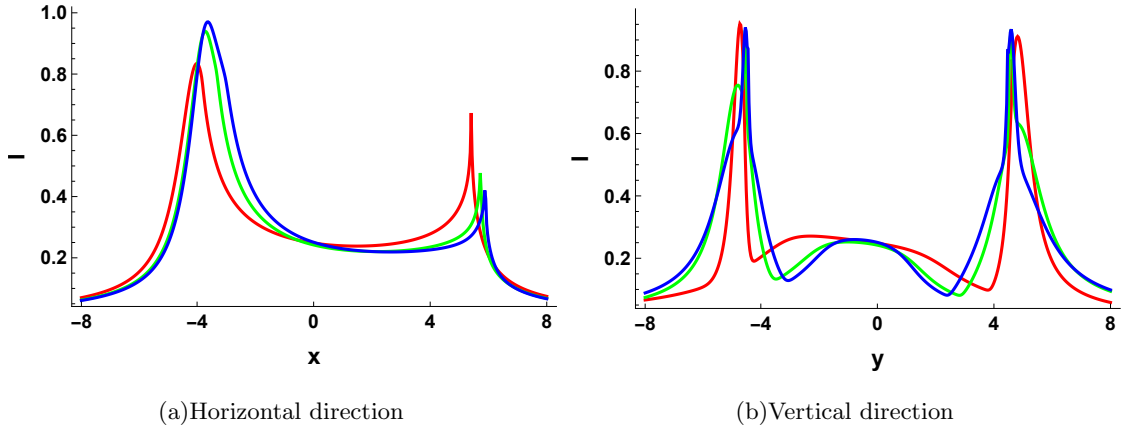


FIG. 5: Intensity distribution for anisotropic radiation under the RIAF model, and the accretion flow follows the infalling motion. The red, green and blue curves corresponds to $\ell = -0.5$, 0.1 and 0.5 , respectively with a fixed $a = 0.6$, $Q = 0.1$, $\theta_o = 75^\circ$.

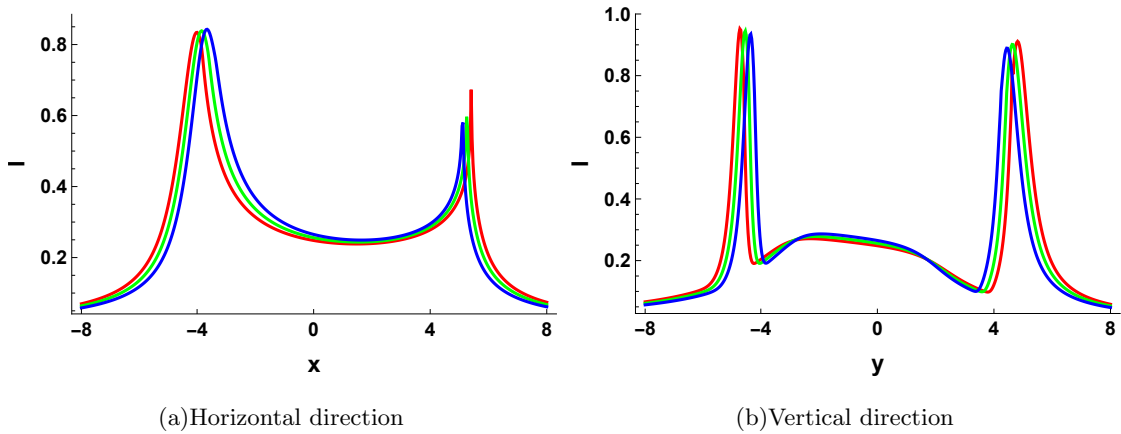


FIG. 6: Intensity distribution for anisotropic radiation under the RIAF model, and the accretion flow follows the infalling motion. The red, green and blue curves corresponds to $Q = 0.1$, 0.3 and 0.5 , respectively with a fixed $a = 0.6$, $\ell = -0.5$, $\theta_o = 75^\circ$.

Now, we extend our analysis to incorporate anisotropic synchrotron emission by assuming a toroidal magnetic field configuration. In Fig. 4, we interpret the corresponding intensity maps of the considering BH model under the RIAF model, at a frequency of 230GHz with an inclination angle of $\theta_o = 75^\circ$, and a spin parameter $a = 0.6$. For quantitative comparison, the horizontal and vertical intensity profiles are depicted in Figs. 5 and 6. In this perspectives, the entire morphology remains qualitatively similar to the isotropic case, as discussed in Fig. 1, characterized by a pronounced bright ring encircling by two central dark regions, both of which slightly reduces with increasing ℓ . Moreover, as Q increases, the resulting image exhibits a slightly asymmetry, characterized by enhanced brightness on the side co-rotating with the BH, due to frame-dragging effects.

A significant feature of the anisotropic case is the observation of a vertically elongated, elliptical ring structure. This asymmetry appears from the angular dependence of synchrotron emissivity: photons emitted from the upper and lower regions of the disk propagate nearly perpendicular to the magnetic field, resulting in slightly enhanced emission and a vertically stretched bright ring.

B. BAAF Model

Now, we discuss the background mechanism of BAAF model, which is proposed by Hou et al. [73, 98]. In this framework, the fluid is assumed to be electrically neutral, with the plasma fully ionized into electrons and protons. The accreting matter is constrained to constant- θ surfaces such as, $u^\theta \equiv 0$. The conservation equation for the mass flow can thus be defined as

$$\frac{d}{dr} (\sqrt{-g} \rho u^r) = 0, \quad (38)$$

with its solution is

$$\rho = \frac{\rho_0}{\sqrt{-g} u^r} \sqrt{-g} u^r \Big|_{r=r_0}, \quad (39)$$

here, $\rho_0 = \rho(r_0)$ is the mass density at the reference point, typically taken as $r_0 = r_+$. The projection of the energy momentum tensor along u^α satisfies

$$d\chi = \frac{\chi + p}{\rho} d\rho, \quad (40)$$

where χ denotes the internal energy of the fluid. Further, the ratio between proton to electron temperature is defined as $U = T_p/T_e$, and the corresponding internal energy under this approximation is

$$\chi = \rho + \frac{3(U + 2)\rho m_e \theta_e}{2m_p}, \quad (41)$$

with $\theta_e = U_B T_e / m_e c^2$ denoting the dimensionless electron temperature. Using the ideal gas law, the pressure is

$$p = n U_B (T_p + T_e) = \frac{(1 + U)\rho m_e \theta_e}{m_p}. \quad (42)$$

Putting Eqs. (41) and (42) into Eq. (40) and integrating gives

$$\theta_e = (\theta_e)_0 \left(\frac{\rho}{\rho_0} \right)^{\frac{2(1+U)}{3(2+U)}}, \quad (43)$$

in which $(\theta_e)_0$ is the reference temperature at r_+ . For computational convenience, we consider that $\rho(r_+, \theta)$ based on a Gaussian distribution in the θ direction and, in the conical solution, take $\theta_e(r_+, \theta)$ to be constant

$$\rho(r_+, \theta) = \rho_h \exp \left[- \left(\frac{\sin \theta - \sin \mu_\theta}{\sigma_\theta} \right)^2 \right], \quad \theta_e(r_+, \theta) = \theta_h, \quad (44)$$

here μ_θ represents the mean position in the θ direction and σ_θ is the standard deviation of the distribution. For M87*, observations indicate $\rho_h \simeq 1.5 \times 10^3 \text{ g cm}^{-1} \text{ s}^{-2}$ and $\Theta_h \simeq 16.86$, corresponding to an electron number density $n_h = 10^6 \text{ cm}^{-3}$ and temperature $T_h = 10^{11} \text{ K}$ [101]. For a spherically symmetric spacetime, the magnetic field configuration simplifies as

$$b^\alpha = \frac{\Psi}{\sqrt{-g}u^r} \left[(u_t + \Omega_b u_\phi) u^\mu + \delta_t^\mu + \Omega_b \delta_\phi^\mu \right], \quad (45)$$

where $\Psi = F_{\theta\phi}$ is a component of the electromagnetic field tensor. Here, we consider a separable monopole solution

$$\Psi = \Psi_0 \text{sign}(\cos \theta) \sin \theta. \quad (46)$$

The angular velocity of the magnetic field is taken as $\Omega_b = 0.3 \Omega_h$, with $\Omega_h = a/(2r_+)$ indicating the spin angular velocity of the BH. In this model, we only consider the anisotropic radiation (25), and the fluid four velocity is still described by the ballistic approximation such as, the fluid moves along geodesics.

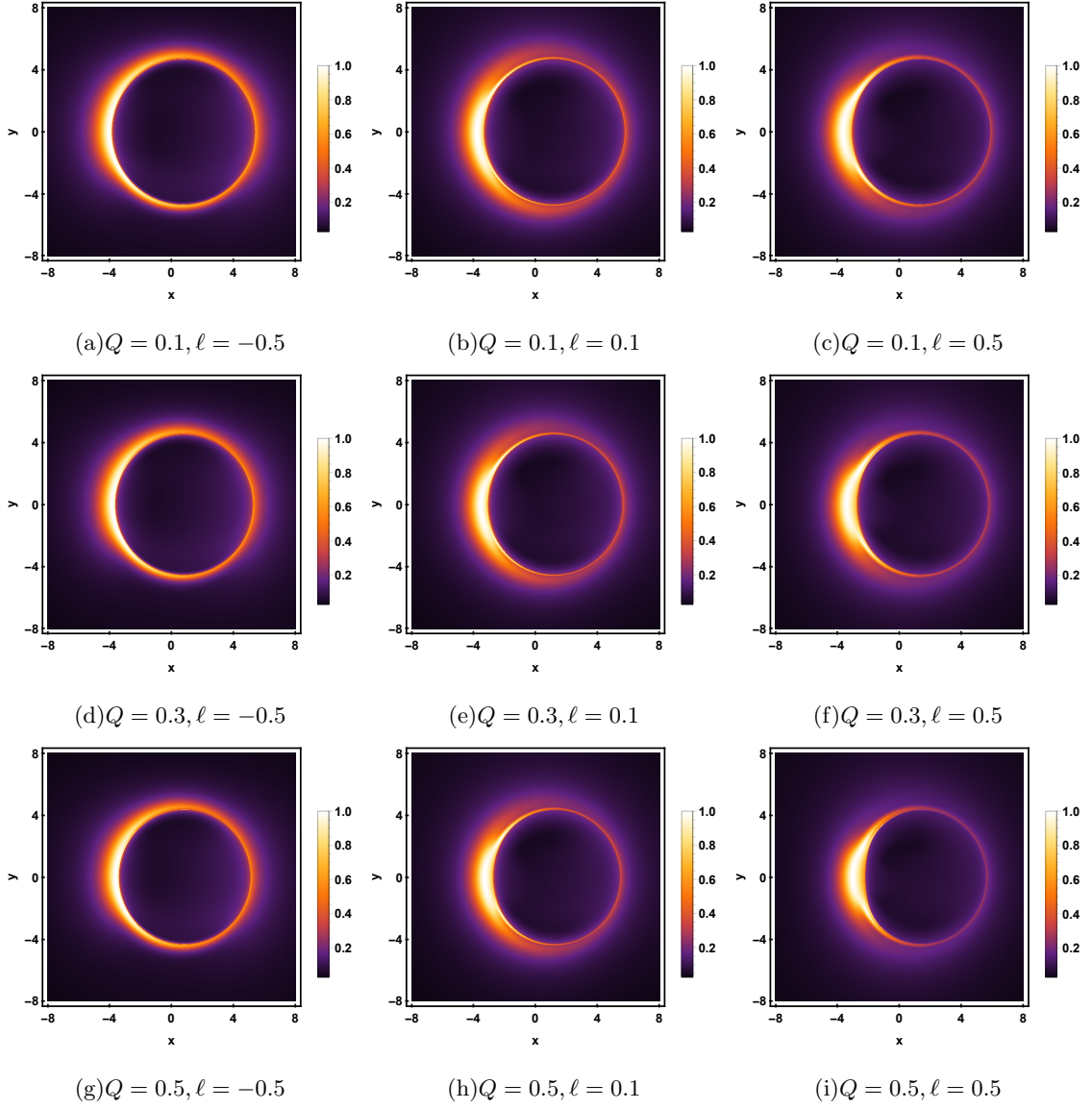


FIG. 7: Imaging results of the thick accretion disk for anisotropic radiation under the BAAF model, and the accretion flow follows the infalling motion. The observation is performed at a frequency of 230GHz with an inclination angle of $\theta_o = 75^\circ$, and a spin parameter $a = 0.6$.

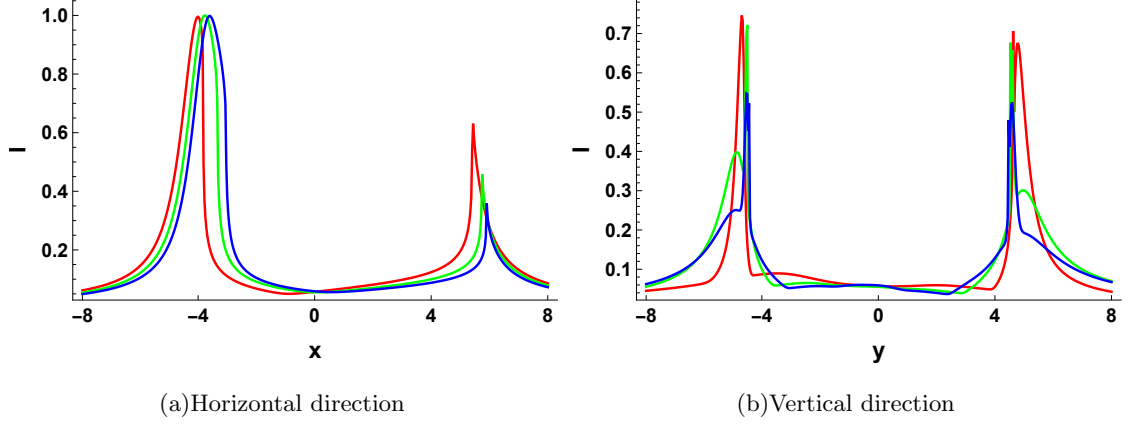


FIG. 8: Intensity distribution for anisotropic radiation under the BAAF model, and the accretion flow follows the infalling motion. The red, green and blue curves corresponds to $\ell = -0.5, 0.1$ and 0.5 , respectively with a fixed $a = 0.6$, $Q = 0.1$, $\theta_o = 75^\circ$.

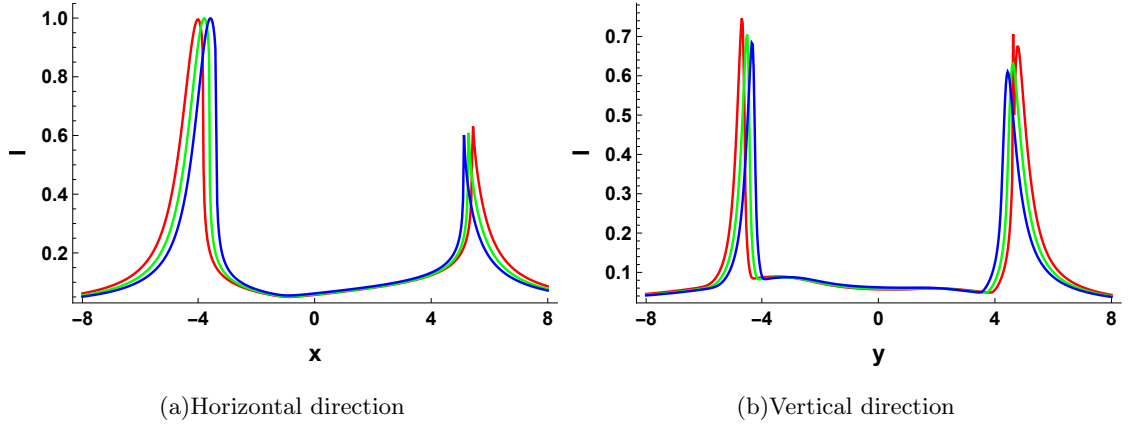


FIG. 9: Intensity distribution for anisotropic radiation under the BAAF model, and the accretion flow follows the infalling motion. The red, green and blue curves corresponds to $Q = 0.1, 0.3$ and 0.5 , respectively with a fixed $a = 0.6$, $\ell = -0.5$, $\theta_o = 75^\circ$.

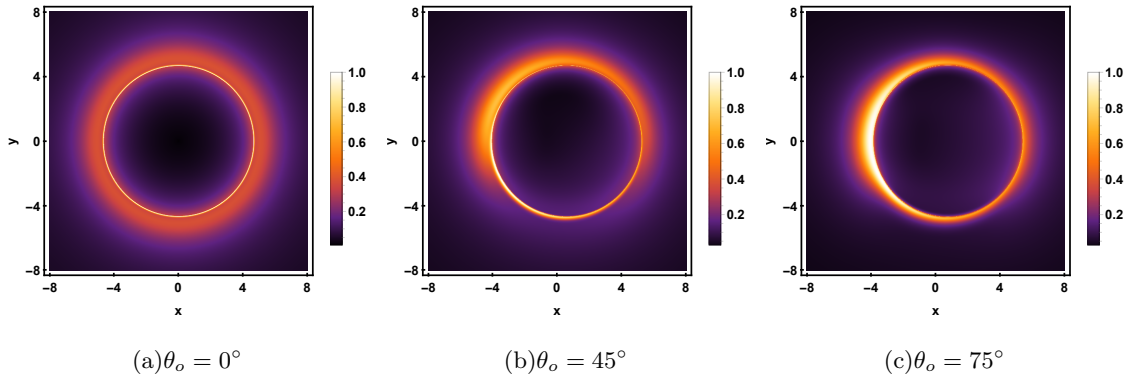


FIG. 10: Imaging results of the thick accretion disk for anisotropic radiation under the BAAF model, and the accretion flow follows the infalling motion. The observation is performed at a frequency of 230GHz with an inclination angles of $\theta_o = 0^\circ$, $\theta_o = 45^\circ$ and $\theta_o = 75^\circ$ from left to right, respectively. For all cases we fixed $a = 0.6$, $\ell = -0.5$ and $Q = 0.1$.

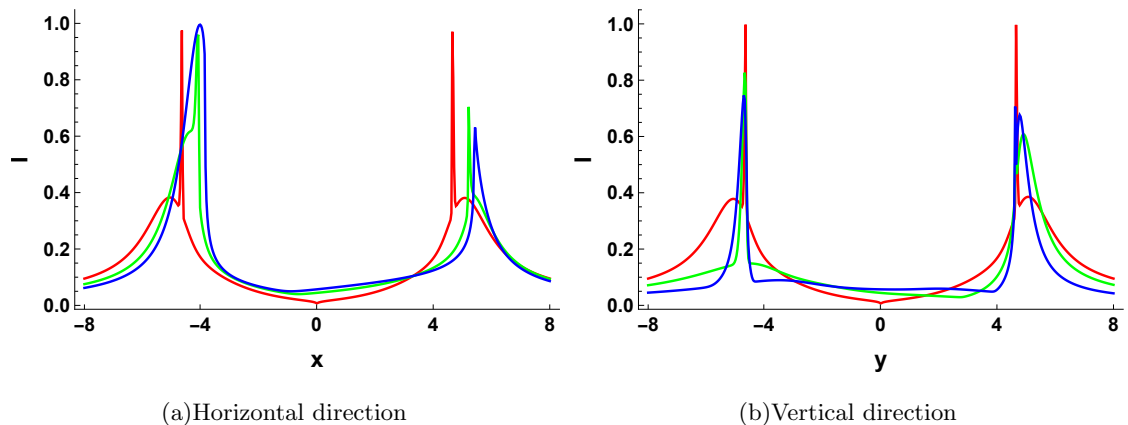


FIG. 11: Intensity distribution for anisotropic radiation under the BAAF model, and the accretion flow follows the infalling motion. The red, green and blue curves corresponds to $\theta_o = 0^\circ$, $\theta_o = 45^\circ$ and $\theta_o = 75^\circ$, respectively with a fixed $a = 0.6$, $\ell = -0.5$, $Q = 0.1$.

In Fig. 7, we exhibit the overall intensity distribution of the Kerr-Sen-like BH within the fabric of the BAAF disk model under anisotropic synchrotron emission. The accretion flow is considered to be purely infalling, and the observation is performed at a frequency of 230GHz. The corresponding horizontal and vertical intensity profiles are depicted in Figs. 8 and 9. Overall, the dependence of the image morphology on the BH LSB parameter ℓ and charge Q , closely parallels the behavior observed in the RIAF case. Nevertheless, several notable differences are observed. Compared with the RIAF framework, as shown in Figs. 1 and 4, the bright ring in the BAAF disk images appears generally thinner, and the separation between the primary and higher-order images becomes more pronounced.

We further presents the variation of the intensity distribution with the alteration of the inclination angles in Fig. 10. The associated horizontal and vertical intensity profiles are displays in Fig. 11, which provides a quantitative comparison of the brightness distributions. For polar viewing, the bright ring and the dark region lies in the centered. At $\theta_o = 0^\circ$, a clear up-down asymmetry in the bright ring emerges. When the inclination increases to $\theta_o = 45^\circ$, the dark region slightly emerge inside the ring, with the upper one significantly thicker, as compared to lower one. At $\theta_o = 75^\circ$, the brightness distribution becomes slightly nonuniform, with a distinct dark region appearing inside the bright ring. Moreover, the left-side brightness are more pronounced, and the bright ring structure are vertically elongated, at large inclinations. This asymmetry appears from the angular dependence of synchrotron emissivity: photons radiated from the upper and lower parts of the disk propagate nearly perpendicular to the magnetic field, resulting in enhanced emission and a vertically stretched ring.

V. POLARIZATION IMAGING

For polarized imaging, we only consider the BAAF model with anisotropic radiation. Based on the WKB approximation, the propagation of light satisfies the covariant radiative transfer equation

$$k^\alpha \nabla_\alpha \mathcal{S}^{\mu\nu} = J^{\mu\nu} + H^{\mu\nu\alpha\varrho} \mathcal{S}_{\alpha\varrho}. \quad (47)$$

Here, k^α represents the photon's wave vector, $\mathcal{S}^{\mu\nu}$ denotes the polarization tensor defining the polarization state of the light, $J^{\mu\nu}$ describes the emission properties of the radiation source, and $H^{\mu\nu\alpha\varrho}$ characterizes the response of the propagation medium to the light ray, including absorption and Faraday's rotation effects [102]. The polarization tensor $\mathcal{S}^{\mu\nu}$ is directly proportional to the photon's polarization density matrix. Subsequently, it is Hermitian, satisfying $\mathcal{S}^{\mu\nu} = \overline{\mathcal{S}^{\nu\mu}}$, in which the overline denotes complex conjugation, and it is gauge invariant. Using this gauge invariance, the calculation can be carried out within a conveniently chosen parallel-transported tetrad frame. The covariant radiative transfer equation (47) can then be classified into two parts. The first part,

$$k^\alpha \nabla_\alpha f^\nu = 0, \quad f_\nu k^\nu = 0, \quad (48)$$

reflects the gravitational effects, where f^ν is a normalized spacelike vector orthogonal to k^ν . The second part corresponds to the radiative transfer along the ray

$$\frac{dS}{d\varpi} = R(\psi)J - R(\psi)MR(-\psi)S, \quad (49)$$

with the matrices defined as

$$\begin{aligned}
 S &= \begin{pmatrix} \mathcal{I} \\ \mathcal{Q} \\ \mathcal{U} \\ \mathcal{V} \end{pmatrix}, & J &= \frac{1}{\nu^2} \begin{pmatrix} j_I \\ j_Q \\ j_U \\ j_V \end{pmatrix}, & M &= \nu \begin{pmatrix} a_I & a_Q & a_U & a_V \\ a_Q & a_I & r_V & -r_U \\ a_U & -r_V & a_I & r_Q \\ a_V & r_U & -r_Q & a_I \end{pmatrix}, \\
 R(\psi) &= \begin{pmatrix} 1 & 0 & 0 & 0 \\ 0 & \cos(2\psi) & -\sin(2\psi) & 0 \\ 0 & \sin(2\psi) & \cos(2\psi) & 0 \\ 0 & 0 & 0 & 1 \end{pmatrix}.
 \end{aligned} \tag{50}$$

where $R(\psi)$ is a rotation matrix. The rotation angle ψ is the angle between the reference vector f^α and the local magnetic field b^α in the transverse plane of the light ray, calculated as [?]]

$$\psi = \text{sign}(\epsilon_{\alpha\beta\rho\sigma} u^\alpha f^\beta b^\rho k^\sigma) \arccos \left(\frac{P^{\alpha\beta} f_\alpha b_\beta}{\sqrt{(P^{\alpha\beta} f_\alpha f_\beta)(P^{\mu\nu} b_\mu b_\nu)}} \right), \tag{51}$$

where $P^{\alpha\beta}$ is the induced metric in the transverse subspace. At the observer, the Stokes parameters are projected onto the observer's screen, again using a rotation matrix. The corresponding rotation angle is

$$\psi_0 = \text{sign}(\epsilon_{\mu\nu\alpha\beta} u^\mu f^\nu d^\alpha k^\beta) \arccos \left(\frac{P^{\alpha\beta} f_\alpha d_\beta}{\sqrt{(P^{\alpha\beta} f_\alpha f_\beta)(P^{\mu\nu} d_\mu d_\nu)}} \right), \tag{52}$$

where d^α is chosen along the y -axis of the screen, $d^\alpha = -\partial_\theta^\alpha$. The projected Stokes parameters are then

$$\mathcal{I}_o = \mathcal{I}, \quad \mathcal{Q}_o = \mathcal{Q} \cos \psi_o - \mathcal{U} \sin \psi_o, \quad \mathcal{U}_o = \mathcal{Q} \sin \psi_o + \mathcal{U} \cos \psi_o, \quad \mathcal{V}_o = \mathcal{V}, \tag{53}$$

where \mathcal{I}_o represents the intensity. The Stokes parameters \mathcal{Q}_o and \mathcal{U}_o are associated with the electric field $\vec{E} = (E_x, E_y)$ by

$$\mathcal{Q}_o = E_x^2 - E_y^2, \quad \mathcal{U}_o = 2E_x E_y. \tag{54}$$

Generally, if \mathcal{U}_o is positive, E_x and E_y have the same sign, and \vec{E} lies in the first or third quadrant; if \mathcal{U}_o is negative, E_x and E_y have opposite signs, and \vec{E} lies in the second or fourth quadrant. The sign of \mathcal{Q}_o indicates whether \vec{E} is aligned closer to the line $y = x$ or $y = -x$. The parameter \mathcal{V}_o characterizes the circular polarization: positive values indicate left-handed circular polarization, while negative values correspond to right-handed circular polarization. From the Stokes parameters, one can determine both the magnitude and orientation of the projected linear polarization

vector \vec{f} on the observer's frame. Specifically, its magnitude gives the degree of linear polarization, whereas its direction defines the electric vector position angle (EVPA)

$$|\vec{f}| = \mathcal{P}_o = \frac{\sqrt{\mathcal{Q}_o^2 + \mathcal{U}_o^2}}{\mathcal{I}_o}, \quad \arg(\vec{f}) = \Phi_{\text{EVPA}} = \frac{1}{2} \arctan\left(\frac{\mathcal{U}_o}{\mathcal{Q}_o}\right). \quad (55)$$

Within this mechanism, the Stokes parameters and the linear polarization vector \vec{f} can be evaluated, enabling a complete characterization of the polarization characteristics.

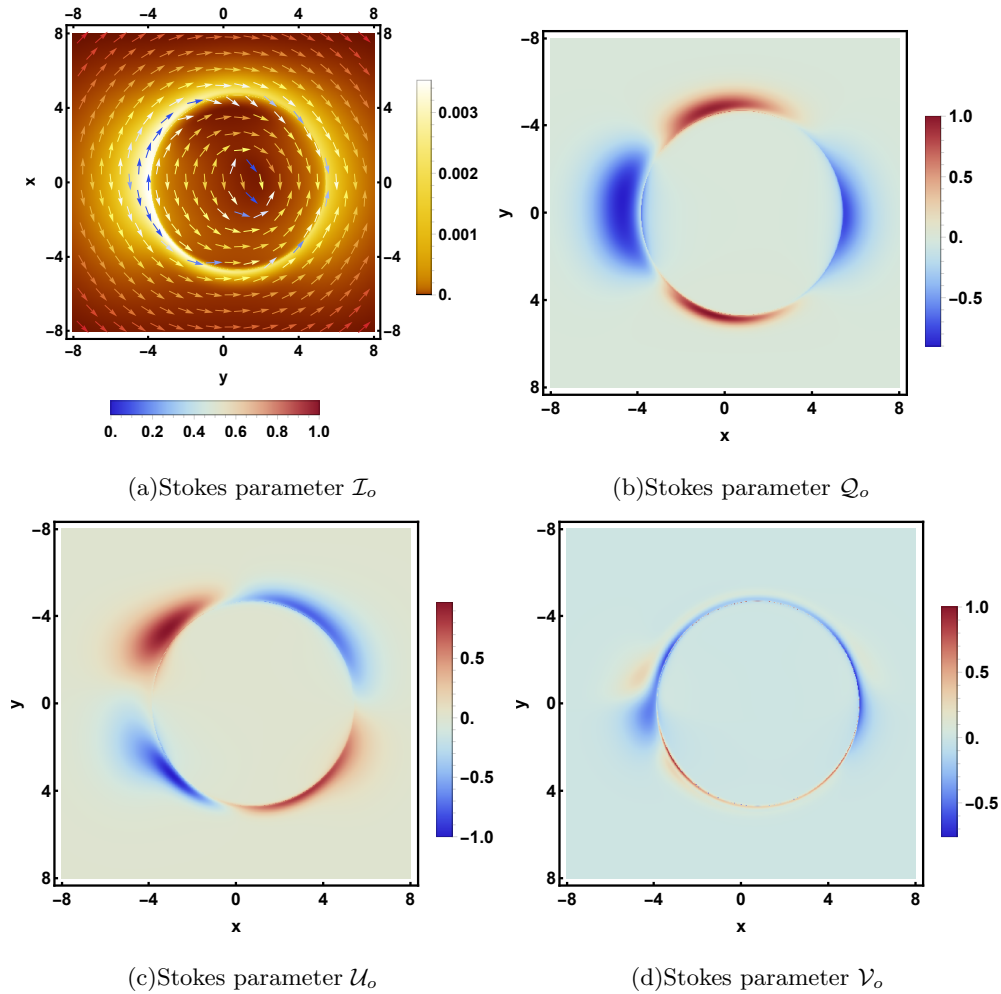


FIG. 12: The resulting Stokes parameters \mathcal{I}_o , \mathcal{Q}_o , \mathcal{U}_o , and \mathcal{V}_o under the BAAF disk model with an infalling motion. The observation is performed at a frequency of 230GHz with an inclination angle of $\theta_o = 75^\circ$, with a fixed $a = 0.6$, $\ell = -0.5$ and $Q = 0.1$.

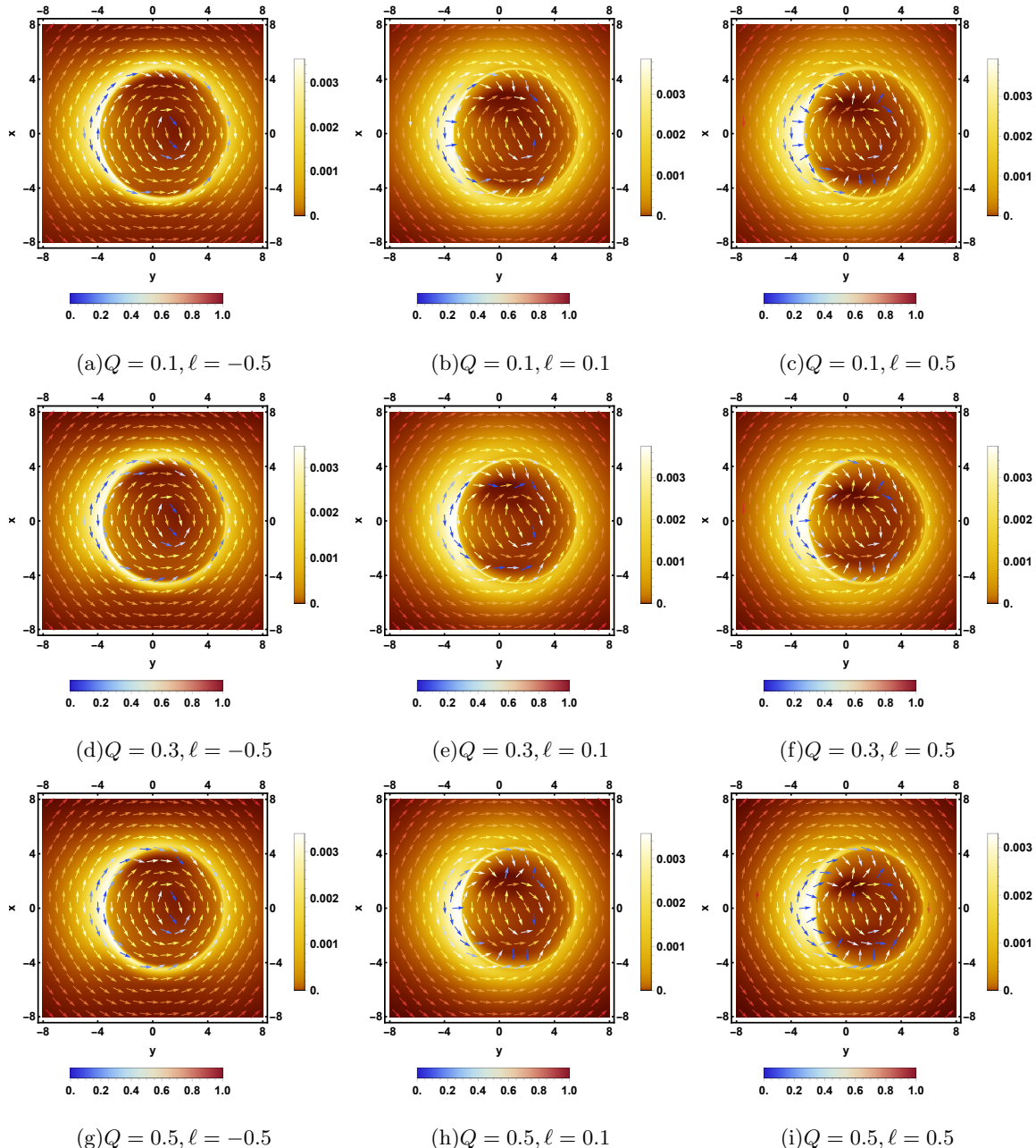


FIG. 13: Polarized images of the Kerr-Sen-like BH in the BAAF model with anisotropic emission. The accretion flow follows the infalling motion, and the observation is performed at a frequency of 230GHz with an inclination angle of $\theta_o = 75^\circ$, and a spin parameter $a = 0.6$.

In Fig. 12, we presents a representative example of the observed Stokes parameters \mathcal{I}_o , Q_o , \mathcal{U}_o , and \mathcal{V}_o under the BAAF disk model with an infalling motion. The observation is performed at a frequency of 230GHz with an inclination angle of $\theta_o = 75^\circ$, with a fixed $a = 0.6$, $\ell = -0.5$ and $Q = 0.1$. The quantity \mathcal{I}_o indicates the intensity distribution. The arrows represents the linear polarization vector \vec{f} , where their color corresponds to the polarization degree \mathcal{P}_o , while

their orientation specifies the EVPA Φ_{EVPA} . Since \vec{f} is always perpendicular to the magnetic field \vec{b} , it can be inferred that the magnetic field is approximately radial. Combining \mathcal{Q}_o and \mathcal{U}_o allows for a qualitative determination of the direction of the electric vector \vec{E} , while $\mathcal{V}_o < 0$ indicates right-handed circular polarization. Closer to the BH event horizon, frame-dragging effects become dominant, causing the magnetic field lines to twist into a more azimuthal configuration. Using the flux-freezing condition of ideal magnetohydrodynamics, the magnetic field remains closely coupled to the plasma motion. Consequently, the observed rotation of the polarization angle serves as a direct signature of the frame-dragging influence of the BH on the accreting plasma. The parameters \mathcal{Q}_o and \mathcal{U}_o reach their maxima closer to the higher-order images and decay rapidly away from this region. The distribution of \mathcal{V}_o indicates right-handed polarization on both sides of the higher-order images, while the remaining regions displays left-handed polarization.

Figure 13 presents the impact of ℓ and Q on the polarization images. In these images, the bright rings correspond to the higher-order images, and the dark region inside originates from the event horizon. The results indicates that as ℓ increases from left to right, the position where the polarization vectors start to exhibit azimuthal twisting moves away from the BH. Meanwhile, by examining each column, we find that as Q increases, the polarization vectors exhibit noticeable changes, while the corresponding polarized intensity within the bright ring becomes increasingly prominent. Overall, both ℓ and Q significantly influence the polarization properties, reflecting the impact of the underlying spacetime structure on the observed polarization behavior.

VI. SUMMARY

In the present study, we revisited the fundamentals of Bumblebee gravity, which yields a Kerr-Sen-like BH metric, and analyzed the visual characteristics surrounded by a geometrically thick accretion flow. We define the background of null geodesics along with the definition of photon sphere, and then provide a comprehensive review of two representative geometrically thick accretion flow models, which is known as the phenomenological RIAF model and the analytical BAAF model. We solve the geodesics and the radiative transfer equations numerically, and observed the corresponding shadow images and polarization structures with observational frequency at 230GHz.

For the RIAF model, both the isotropic and anisotropic radiation frameworks are investigated, with the accretion flow mode being the infalling motion for various values of LSB parameter ℓ and charge Q with an inclination angle of $\theta_o = 75^\circ$. The obtained results show that, in isotropic radiation scenarios, increasing Q slightly decreases both the size and brightness of the higher-order

image, while increasing ℓ alters the shape of the higher-order image and obscures the horizon's boundary. Moreover, the image is nearly symmetric in the vertical direction, although the left-right intensity remains higher than the top-bottom intensity. Interestingly, at smaller values of $\ell = 0.1$, two dark regions appear inside the higher-order image, with the upper region slightly darker than the lower one, which is more obvious with increasing ℓ . This phenomenon arises from gravitational lensing effects. We further examined the anisotropic synchrotron emission by imposing a toroidal magnetic field configuration. The overall morphology remains qualitatively similar to the isotropic case, as characterized by a pronounced bright ring encircled by two central dark regions, both of which slightly reduce with increasing ℓ . A significant feature is observed that the brightness distribution exhibits a slight asymmetry for higher values of Q , characterized by enhanced brightness on the side co-rotating with the BH, due to frame-dragging effects. The bright ring appears vertically elongated and slightly elliptical, reflecting the geometry of the underlying magnetic field configuration.

We further analyzed the imaging and polarization properties of the BAAF disk model. For the intensity distribution, we again assume purely infalling matter with anisotropic synchrotron radiation, allowing for a direct comparison with the RIAF model. The resulting intensity maps display a relatively narrower bright ring and a more pronounced dark central region than those obtained in the RIAF case. This distinction can be attributed to the fact that, for certain parameter regimes, the BAAF disk within the conical approximation becomes geometrically thinner than the corresponding RIAF disk in some regions. For the polarization images of the BAAF model, both the LSB parameter ℓ and the BH charge Q play a crucial role in shaping the magnitude and orientation of the polarization vectors. This suggests that polarization images of the considered BH model can serve as an effective probe of the underlying spacetime geometry. Moreover, in contrast to thin-disk scenarios, gravitational lensing of radiation originating from off-equatorial regions produce a wider spread of polarization vectors across the image plane. As a result, thick-disk models exhibit richer and more intricate polarization signatures.

In conclusion, this work main physical parameters of a BH strongly influence the intricate properties of its shadow in geometrically thick, optically thin accretion flows. These configurations provide a more realistic description of astrophysical environments compared to idealized thin disk models. A combined analysis of intensity and polarization images enables a more complete understanding of both the emitted radiation properties and the surrounding spacetime geometry. Looking ahead, it would be worthwhile to extend this framework to other compact objects, such as neutron stars and boson stars, to identify distinguishing observational features among different

gravitational systems. We hope that these investigations could provide useful theoretical benchmarks for future high resolution astronomical observations.

Acknowledgements

This work is supported by the National Natural Science Foundation of China (Grants Nos. 12375043, 12575069), and Chongqing Normal University Fund Project (Grants No. 26XLB001). Princess Nourah bint Abdulrahman University Researchers Supporting Project number (PNURSP2026R59), Princess Nourah bint Abdulrahman University, Riyadh, Saudi Arabia.

-
- [1] K. Akiyama et al., *Astrophys. J. Lett.* **875**, L1 (2019).
 - [2] K. Akiyama et al., *Astrophys. J. Lett.* **910**, L12 (2021).
 - [3] K. Akiyama et al., *Astrophys. J. Lett.* **930**, L12 (2022).
 - [4] K. Akiyama et al., *Astrophys. J. Lett.* **964**, L25 (2024).
 - [5] M. Bauböck et al., *Astron. Astrophys.* **635**, (2020) A143.
 - [6] R. Abuter et al., *Astron. Astrophys.* **677**, (2023) L10.
 - [7] M. D. Johnson et al., *Sci. Adv.* **6** (2020) eaaz1310.
 - [8] R. Gold et al., *Astrophys. J.* **897** (2020) 148.
 - [9] P.O. Mazur, *Black hole uniqueness theorems*, hep-th/0101012.
 - [10] C. M. Will, *Living Rev. Rel.* **17** (2014) 4.
 - [11] K. Yagi and L.C. Stein, *Class. Quant. Grav.* **33** (2016) 054001.
 - [12] R.P. Kerr, *Phys. Rev. Lett.* **11** (1963) 237.
 - [13] R. Penrose, *Phys. Rev. Lett.* **14** (1965) 57.
 - [14] C. Bambi, *Mod. Phys. Lett. A* **26** (2011) 2453.
 - [15] V. Cardoso and P. Pani, *Living Rev. Rel.* **22** (2019) 4.
 - [16] V. A. Kostelecky, *Phys. Rev. D* **69** (2004) 105009.
 - [17] C. Ding, X. Chen and X. Fu, *Nucl. Phys. B* **975** (2022) 115688.
 - [18] V. A. Kostelecky and S. Samuel, *Phys. Rev. D* **39** (1989) 683.
 - [19] T. Jacobson, S. Liberati and D. Mattingly, *Annals Phys.* **321** (2006) 150.
 - [20] V. A. Kostelecký and M. Mewes, *Phys. Lett. B* **757** (2016) 510.
 - [21] D. Colladay and V. A. Kostelecký, *Phys. Rev. D* **58** (1998) 116002.
 - [22] V. A. Kostelecký and S. Samuel, *Phys. Rev. Lett.* **63** (1989) 224.
 - [23] A. V. Kostelecký and J. D. Tasson, *Phys. Rev. D* **83** (2011) 016013.
 - [24] R. Casana, et al., *Phys. Rev. D* **97** (2018) 104001.
 - [25] I. Güllü and A. Övgün, *Annals Phys.* **436** (2022) 168721.
 - [26] Q. G. Bailey, et al., *Phys. Rev. D* **112** (2025) 024069.
 - [27] C. Ding, C. Liu, R. Casana and A. Cavalcante, *Eur. Phys. J. C* **80** (2020) 178.

- [28] C. Ding and X. Chen, *Chin. Phys. C* **45** (2021) 025106.
- [29] A. Sen, *Phys. Rev. Lett.* **69** (1992) 1006.
- [30] S. K. Jha and A. Rahaman, *Eur. Phys. J. C* **81** (2021) 345.
- [31] R. Xu, D. Liang, and L. Shao, *Phys. Rev. D* **107** (2023) 024011.
- [32] X. Zhu, R. Xu, and D. Xu, arXiv:2411.18559.
- [33] S. K. Jha, S. Aziz, and A. Rahaman, *Eur. Phys. J. C* **82** (2022) 106.
- [34] Z. Wang, S. Chen, and J. Jing, *Eur. Phys. J. C* **82** (2022) 528.
- [35] S. U. Islam, S. G. Ghosh, and S. D. Maharaj, *JCAP* **12** (2024) 047.
- [36] J. Gu. et al., *Eur. Phys. J. C* **82** (2022) 708.
- [37] H. Y. YuChih, and Y. Shen, *Phys. Rev. D* **112** (2025) 104016.
- [38] J. P. Zhang, Y. Zhang, and L. Han, arXiv:2604.23721.
- [39] J. Zhu and H. Li, arXiv:2604.09464.
- [40] F. Ahmed, S. Kala and E. O. Silva, arXiv:2604.00883.
- [41] S. Capozziello, et al., *JCAP* **2023** (2023) 027.
- [42] G. Lambiase, et al., *JCAP* **2023** (2023) 026.
- [43] R. D. Blandford and R. L. Znajek, *Mon. Not. Roy. Astron. Soc.* **179** (1977) 433.
- [44] R. Narayan, M. D. Johnson, and C. F. Gammie, *Astrophys. J. Lett.* **885** (2019) L33.
- [45] X. X. Zeng, H. Q. Zhang and H. Zhang, *Eur. Phys. J. C* **80** (2020) 872.
- [46] X. X. Zeng, M. I. Aslam, R. Saleem, *Eur. Phys. J. C* **83** (2023) 129.
- [47] R. Saleem and M. I. Aslam, *Eur. Phys. J. C* **83** (2023) 257.
- [48] M. I. Aslam and R. Saleem, *Eur. Phys. J. C* **84** (2024) 37.
- [49] S. Guo et al., *Astrophys. J.* **975** (2024) 237.
- [50] C. Y. Yang, M. I. Aslam and X. X. Zeng, et al., *J. High Energy Astrophys.* **46** (2025) 100345.
- [51] X. X. Zeng, C. Y. Yang and M. I. Aslam, et al., *J. Cosmol. Astropart. Phys.* **2025** (2025) 066.
- [52] G.-P. Li and K.-J. He, *JCAP* **06** (2021) 037.
- [53] X. X. Zeng et al., *J. High Energy Astrophys.* **51** (2026) 100540.
- [54] M. I. Aslam et al., arXiv:2604.18628.
- [55] K. Hashimoto, S. Kinoshita and K. Murata, *Phys. Rev. D* **101**, 066018 (2020).
- [56] X. Y. Hu, M. I. Aslam and R. Saleem et al., *J. Cosmol. Astropart. Phys.* **2023** (2023) 013.
- [57] M. I. Aslam, X. X. Zeng and R. Saleem et al., *Chin. Phys. C* **48** (2024) 115101.
- [58] X. X. Zeng, M. I. Aslam and R. Saleem et al., *Eur. Phys. J. C* **85** (2025) 663.
- [59] R. Narayan and I.-s. Yi, *Astrophys. J. Lett.* **428** (1994) L13.
- [60] F. Yuan and R. Narayan, *Ann. Rev. Astron. Astrophys.* **52** (2014) 529.
- [61] R. Narayan, I. Yi, and R. Mahadevan, *Nature* **374** (1995) 623.
- [62] O. Porth et al., *Astrophys. J. Suppl.* **243** (2019) 26.
- [63] H.-X. Jiang et al., *JCAP* **01** (2024) 059.
- [64] A. Uniyal et al., *Astrophys. J.* **993** (2025) 97.

- [65] F. Yuan, E. Quataert and R. Narayan, *Astrophys. J.* **598**, 301 (2003).
- [66] A. Broderick and A. Loeb, *Astrophys. J.* **697**, 1164 (2009).
- [67] H. Y. Pu and A. E. Broderick, *Astrophys. J.* **863**, 148 (2018).
- [68] H. X. Jiang et al., *JCAP* **01**, 059 (2024).
- [69] F. C. Michel, *Astrophys. Space Sci.* **15** (1972) 153.
- [70] T. Manmoto, *Astrophys. J.* **534** (2000) 734.
- [71] E. Tejeda, P. A. Taylor and J. C. Miller, *Mon. Not. Roy. Astron. Soc.* **429** (2013) 925.
- [72] R. K. Ulrich, *Astrophys. J.* **210** (1976) 377.
- [73] Y. Hou, Z. Zhang, M. Guo, and B. Chen, *JCAP* **02** (2024) 030.
- [74] S. Guo et al., *Eur. Phys. J. C* **84** (2024) 601.
- [75] K. Akiyama et al., *Astrophys. J. Lett.* **910** (2021) L12
- [76] K. Akiyama et al., *Astrophys. J. Lett.* **964** (2024) L25.
- [77] A. M. Beloborodov, *Astrophys. J. Lett.* **566** (2002) L85-L88.
- [78] K. Akiyama et al., *Astrophys. J.* **912** (2021) 35.
- [79] X. Wang et al., *Phys. Rev. D* **113**, 024033 (2026).
- [80] B. Chen, Y. Hou, Y. Song and Z. Zhang, *Phys. Rev. D* **111**, 083045 (2025).
- [81] Y. Hou et al., *Astrophys. J. Lett.* **988**, L51 (2025).
- [82] X. X. Zeng, C. Y. Yang, H. Yu and K. J. He, *Eur. Phys. J. C* **86**, 169 (2026).
- [83] C. Y. Yang, K. J. He, X. X. Zeng and L. F. Li, arXiv:2508.07393.
- [84] H. Yin, S. Chen and J. Jing, arXiv:2507.03857.
- [85] C. Y. Yang, H. Ye and X. X. Zeng, *Eur. Phys. J. C* **86**, 370 (2026).
- [86] X. Wang, Y. Wang and X. X. Zeng, arXiv:2510.17906.
- [87] X. X. Zeng, et al., *Eur. Phys. J. C* **86**, 383 (2026).
- [88] M. I. Aslam, et al., *J. High Energy Astrophys.* **51**, 100551 (2026).
- [89] X. X. Zeng, et al., arXiv:2603.07185.
- [90] C. Y. Yang and X. X. Zeng, arXiv:2604.00117.
- [91] Q. Wan, Y. Hou and M. Guo, *Phys. Rev. D* **113** (2026) 083023.
- [92] S. Chandrasekhar, *The mathematical theory of black holes*, Oxford University Press, Oxford, U.K. (1998).
- [93] N. Tsukamoto, Z. Li and C. Bambi, *JCAP* **2014** (2014) 043.
- [94] R. Gold, A. E. Broderick, Z. Younsi, C. M. Fromm, C. F. Gammie, M. Mościbrodzka, H. Y. Pu, T. Bronzwaer, J. Davelaar and J. Dexter, et al., *Astrophys. J.* **897**, 148 (2020).
- [95] R. Mahadevan, R. Narayan and I. Yi, *Astrophys. J.* **465**, 327 (1996).
- [96] P. K. Leung, C. F. Gammie, and S. C. Noble, *Astrophys. J.* **737**, 21 (2011).
- [97] A. E. Broderick, V. L. Fish, S. S. Doeleman, and A. Loeb, *Astrophys. J.* **735**, 110 (2011).
- [98] Z. Zhang, Y. Hou, M. Guo, and B. Chen, *JCAP* **05** (2024) 032.
- [99] H.-Y. Pu, K. Akiyama, and K. Asada, *Astrophys. J.* **831** (2016) 4.

- [100] A. Chael, M. D. Johnson and A. Lupsasca, *Astrophys. J.* **918**, 6 (2021).
- [101] F. H. Vincent, S. E. Gralla, A. Lupsasca, and M. Wielgus, *Astron. Astrophys.* **667** (2022) A170.
- [102] J. Huang, L. Zheng, M. Guo and B. Chen, *JCAP* **11**, 054 (2024).